


## Article

# Constructing the Mo<sub>2</sub>C@MoO<sub>x</sub> Heterostructure for Improved SERS Application

Kui Lai <sup>1,2</sup>, Kaibo Yuan <sup>2</sup>, Qinli Ye <sup>2</sup>, Anqi Chen <sup>1,\*</sup>, Dong Chen <sup>2,\*</sup>, Da Chen <sup>2</sup> and Chenjie Gu <sup>1,2</sup> 

<sup>1</sup> The Research Institute of Advanced Technologies, Ningbo University, No. 818 Fenghua Road, Ningbo 315211, China; laikui18839135662@163.com (K.L.); guchenjie@nbu.edu.cn (C.G.)

<sup>2</sup> School of Physical Science and Technology, Ningbo University, No. 818 Fenghua Road, Ningbo 315211, China; 15836294399@163.com (K.Y.); yql1511362567@126.com (Q.Y.); chenda@nbu.edu.cn (D.C.)

\* Correspondence: chenanqi@nbu.edu.cn (A.C.); chendong@nbu.edu.cn (D.C.)

**Abstract:** Surface-enhanced Raman scattering (SERS) is a non-destructive spectra analysis technique. It has the virtues of high detectivity and sensitivity, and has been extensively studied for low-trace molecule detection. Presently, a non-noble-metal-based SERS substrate with excellent enhancement capabilities and environmental stability is available for performing advanced biomolecule detection. Herein, a type of molybdenum carbide/molybdenum oxide (Mo<sub>2</sub>C@MoO<sub>x</sub>) heterostructure is constructed, and attractive SERS performance is achieved through the promotion of the charge transfer. Experimentally, Mo<sub>2</sub>C was first prepared by calcinating the ammonium molybdate tetrahydrate and gelatin mixture in an argon atmosphere. Then, the obtained Mo<sub>2</sub>C was further annealed in the air to obtain the Mo<sub>2</sub>C@MoO<sub>x</sub> heterostructure. The SERS performance was evaluated by using a 532 nm laser as an excitation source and a rhodamine 6G (R6G) molecule as the Raman reporter. This process demonstrates that attractive SERS performance with a Raman enhancement factor (EF) of  $1.445 \times 10^8$  (R6G@ $10^{-8}$  M) and a limit of detection of  $10^{-8}$  M can be achieved. Furthermore, the mechanism of SERS performance improvement with the Mo<sub>2</sub>C@MoO<sub>x</sub> is also investigated. HRTEM detection and XPS spectra reveal that part of the Mo<sub>2</sub>C is oxidized into MoO<sub>x</sub> during the air-annealing process, and generates metal–semiconductor mixing energy bands in the heterojunction. Under the Raman laser irradiation, considerable hole–electron pairs are generated in the heterojunction, and then the hot electrons move towards MoO<sub>x</sub> and subsequently transfer to the molecules, which ultimately boosts the Raman signal intensity.

**Keywords:** SERS; molybdenum carbide; molybdenum oxide; heterojunctions; charge transfer



**Citation:** Lai, K.; Yuan, K.; Ye, Q.; Chen, A.; Chen, D.; Chen, D.; Gu, C. Constructing the Mo<sub>2</sub>C@MoO<sub>x</sub> Heterostructure for Improved SERS Application. *Biosensors* **2022**, *12*, 50. <https://doi.org/10.3390/bios12020050>

Received: 27 December 2021

Accepted: 18 January 2022

Published: 19 January 2022

**Publisher's Note:** MDPI stays neutral with regard to jurisdictional claims in published maps and institutional affiliations.



**Copyright:** © 2022 by the authors. Licensee MDPI, Basel, Switzerland. This article is an open access article distributed under the terms and conditions of the Creative Commons Attribution (CC BY) license (<https://creativecommons.org/licenses/by/4.0/>).

## 1. Introduction

Surface-enhanced Raman spectroscopy (SERS) is a single-molecule analytical technique that can detect and identify chemical and biological compounds through their unique Raman vibration fingerprints [1]. Presently, it has been widely implemented in the fields of bio-medicine, homeland security, food safety, and medical diagnosis, etc. [2–6]. Although the exact mechanism of the enhancement effect is still under debate, the presence of an electromagnetic mechanism (EM) and a chemical mechanism (CM) are two commonly accepted enhancement theories [7]. Generally, the EM relies on the generation of surface plasmon resonance (SPR) on the noble metal-based SERS substrates, which subsequently amplifies the oscillating dipoles of the molecules and ultimately produces the enhanced Raman signal intensity. On the other hand, the CM relies on the photo-induced charge transfer between the molecules and the SERS substrate. The extra charges amplify the polarizability of the molecules, and consequently enhance the Raman signal intensity. Typically, the enhancement factor (EF) produced by the EM can reach  $10^6$  or even higher, whereas it is only around 10–1000 times that obtained on the conventional CM-dependent SERS substrates [8,9].

Up to today, an enormous number of studies on noble metal-based (Au, Ag, and Cu) SERS substrates have been performed. By designing and preparing noble metal-based nanostructures with various morphologies or compositions, fantastic SERS performance has been demonstrated [10–12]. At present, it is well accepted that precise control of the noble metal morphologies and compositions is a major necessity for generating strong plasmonic coupling; however, manufacturing the large-scale nanostructures with high accuracy requires excessive cost. In addition, noble metals generally exhibit poor stability and biocompatibility; thus, SERS detectors prepared with noble metals are rarely used in biological applications [9].

Recently, a non-noble-metal-based SERS substrate has attracted an enormous amount of attention [13–16]. Significantly, molybdenum-based materials, such as molybdenum disulfide ( $\text{MoS}_2$ ), molybdenum telluride ( $\text{MoTe}_2$ ), and molybdenum sub-oxide ( $\text{MoO}_x$ ), show promising SERS performance, which results from the exceptional charge transfer capability caused by the defects in the material [17–19]. For example, a kind of two-dimensional molybdenum disulfide ( $\text{MoS}_2$ ) was used to construct the nonmetallic SERS-based immunoassay. In addition, a desirable EF of  $10^5$  was obtained by the efficient charge transfer resonances induced by the 532 nm laser excitation, which has been ascribed to the effective enrichment of molecules on the large active surfaces of  $\text{MoS}_2$  [20]. Meanwhile, a metallic  $\text{MoO}_2$  was prepared via the hydrothermal method, and the evaluation of its SERS performance revealed that an EF of  $3.75 \times 10^6$  can be achieved due to the excellent charge transfer capability of the  $\text{MoO}_2$  [21]. On the other hand, recent studies have also introduced heterojunctions to promote the charge transfer on the non-noble-metal-based SERS substrate, and they have shown that heterojunction tends to help to efficiently transfer the photo-generated free carriers to the molecules, which significantly improves the SERS performance. Specifically, defective molybdenum oxide/tungsten oxide ( $\text{MoO}_x/\text{WO}_x$ ) are prepared, then they are mixed with different weight ratios to construct the nano-heterojunctions. This shows that an attractive EF of  $10^8$  can be obtained on the substrate with optimal mixing ratios [22]. However, tungsten suboxide suffers from issues of environment instability when the above method is used in a harsh condition or when the material is kept in the air for a long time [23]. At this point, it is notable that improving the charge transfer between the molecules and substrates is a key factor for promoting the SERS performance of the non-noble-metal-based substrate. Moreover, the environmental stability of the SERS substrate material is also essential for various detection applications.

Herein, a molybdenum carbide/molybdenum oxide ( $\text{Mo}_2\text{C}@\text{MoO}_x$ ) heterostructure is constructed to promote its charge transfer for SERS applications. Experimentally,  $\text{Mo}_2\text{C}$  was first prepared by calcinating the ammonium molybdate tetrahydrate and gelatin mixture in an argon atmosphere. Then, the obtained  $\text{Mo}_2\text{C}$  was oxidized in the air to obtain the  $\text{Mo}_2\text{C}@\text{MoO}_x$  heterostructure. The SERS performance was evaluated by using a 532 nm laser as the excitation source and a rhodamine 6G (R6G) molecule as the Raman reporter. Attractive SERS performance with a Raman enhancement factor (EF) of  $1.445 \times 10^8$  ( $\text{R6G}@10^{-8}$  M) and a limit of detection of  $10^{-8}$  M was achieved. Furthermore, the SERS performance improvement of the  $\text{Mo}_2\text{C}@\text{MoO}_x$  is also investigated. High-resolution TEM detection and XPS spectra reveal that part of the  $\text{Mo}_2\text{C}$  is oxidized into  $\text{MoO}_x$  during the air-annealing process, and generates high levels of metal–semiconductor mixing energy in this hetero-region. Under Raman laser irradiation, the enhanced light absorption produces substantial electron–hole pairs in the hetero-region, and then these electrons move towards the molecules because of the  $\text{MoO}_x$  energy level, which ultimately boosts the Raman signal intensity.

## 2. Materials and Methods

### 2.1. Chemicals

Commercial  $\text{Mo}_2\text{C}$  (CAS No.: 12069-89-5, 99.95%) was purchased from Maclin Biochemical Co., Ltd., Shanghai, China. Gelatin (CAS No.: 9000-70-8, 99%) was obtained from Macklin Biochemical Co., Ltd., Shanghai, China. Ammonium molybdate tetrahydrate (CAS

No.: 12054-85-2, AHM, >99%) was purchased from Sinopharm Chemical Reagent Co., Ltd., Shanghai, China. All chemicals were used without further purification. Deionized water (resistivity of 18.2 M $\Omega$ •cm) was used to prepare the solutions in all the experiments.

## 2.2. Synthesis of Mo<sub>2</sub>C

To obtain the Mo<sub>2</sub>C, in the experiment, gelatin (1 g) was first added into deionized water (20 mL), and then AHM (2 g) was put into the solution. After that, the above mixture was stirred vigorously in a 50 °C water bath for 2 h. Thereafter, the prepared solution was dried in the oven to drive the excessive water out at 80 °C for another 25 h. Next, the mixture was dehydrated at 200 °C in the quartz tube with argon flushing for 1 h. Thereafter, the temperature of the quartz tube was raised to 900 °C by 10 °C/min, and held at that temperature for another 1 h. Finally, the quartz tube was cooled down naturally. In the entire carbonization process, the argon gas flow was kept at 45 mL/min. The obtained black solid products were washed and centrifuged with distilled water several times to remove the residue of the reactants, and finally dried in vacuum at 80 °C for further use.

## 2.3. Preparing the Mo<sub>2</sub>C@MoO<sub>x</sub> Films

The obtained Mo<sub>2</sub>C powder was dispersed in alcohol, and ultrasonicated for 15 min. Then, 10  $\mu$ L of the mixed solution was dropped onto the silicon wafer that was pretreated with the piranha solution and dried in the air. Finally, the silicon wafer was transferred to the hot plate for annealing. The optical image and cross-section SEM image of the prepared substrate are shown in Figure S1. It can be observed that the physical thickness of the Mo<sub>2</sub>C is about 78.7 nm.

## 2.4. Measurements and Characterization

X-ray diffraction (XRD) spectra were recorded on a D8 Advance diffractometer equipped with a Lynxeye Xe detector (Bruker AXS, Karlsruhe, Germany). X-ray photoelectron spectroscopy (XPS) was measured with a thermal K- $\alpha$  instrument, the X-ray emission source is Al-K- $\alpha$  rays ( $h\nu \approx 1486.6$  eV), and the experimental binding energy data are corrected to C 1 s = 284.8 eV. The scanning electron microscope (SEM) images of the prepared material were detected on an SU-70 field emission scanning electron microscope (SU-70, Hitachi, Japan) under an accelerating voltage of 5 kV. For the transmission electron microscopy (TEM), high-resolution TEM images were obtained using the transmission electron microscope (Tecnai G2F20S-Twin, FEI, Hillsboro, OR, USA) under an accelerating voltage of 200 kV. UV-vis spectra were recorded on the spectrometer (TU1901, P-General, Samutprakarn, Thailand). The SERS performance was examined using a ProSp-Micro40-VIS Raman system (Hangzhou SPL, Hangzhou, China), and QE Pro spectrometer (QE pro, Ocean Optics, Dunedin, FL, USA) was used to record the Raman spectra. The excitation laser wavelength was 532 nm and the power on the substrate was 1 mW. Meanwhile, the integration time was set to 10 s, and the objective lens was 50 $\times$ .

## 3. Results and Discussion

The black Mo<sub>2</sub>C powder was first detected via SEM. Figure 1a,b shows the microscopic morphologies of the Mo<sub>2</sub>C at different magnifications. It can be seen that the Mo<sub>2</sub>C nanoflakes are in irregular shapes, and the surface of the nanoflakes is relatively smooth. The size of a typical nanoflake is about 87  $\times$  120 nm<sup>2</sup>. The crystal structure of Mo<sub>2</sub>C was then identified via XRD. Figure 1c shows that sharp diffraction peaks can be determined, which indicates that the prepared Mo<sub>2</sub>C has good crystallinity. Then, the SERS performance of the synthesized Mo<sub>2</sub>C was evaluated by using the R6G as the Raman reporter. As Figure 1d shows, the characteristic Raman vibrational peaks can be observed when a 10<sup>-4</sup> M R6G solution is used. However, when the R6G concentration is reduced to 10<sup>-5</sup> M, the Raman peak intensities reduce significantly, and the Raman peaks even become completely extinct when the concentration of R6G solution reaches 10<sup>-6</sup> M (see inset of Figure 1d). Based on the above observation, it is evident that the SERS performance

of the synthesized  $\text{Mo}_2\text{C}$  is extremely weak, which could be ascribed to the weak charge transfer capability from the substrate to the molecules.

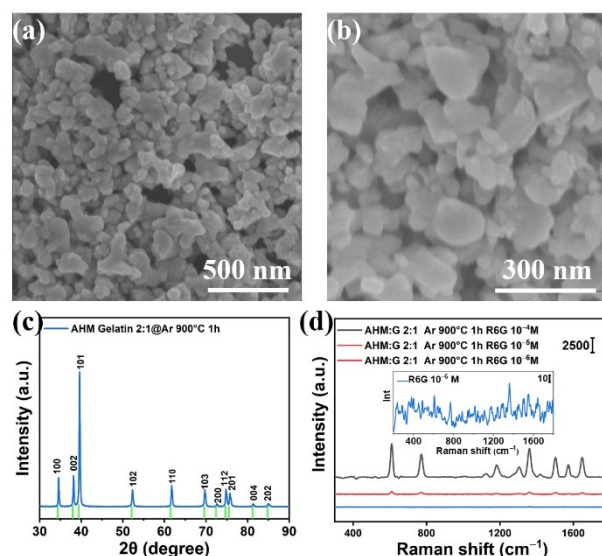


**Figure 1.** (a,b) The SEM images of the synthesized  $\text{Mo}_2\text{C}$  with different magnifications; (c) the XRD spectrum of the synthesized  $\text{Mo}_2\text{C}$ ; (d) the SERS spectra of R6G measured on the synthesized  $\text{Mo}_2\text{C}$ .

In order to improve the SERS performance of the synthesized  $\text{Mo}_2\text{C}$ , the  $\text{Mo}_2\text{C}@\text{MoO}_x$  heterostructure was constructed by annealing the  $\text{Mo}_2\text{C}$  powder in the air. Firstly, three sets of  $\text{Mo}_2\text{C}$  powder were subjected to air annealing at 300 °C, 350 °C, and 400 °C, with the time fixed at 30 min. The UV–vis absorption spectra of the products were collected, and these are shown in Figure 2a. The figure shows that the synthesized  $\text{Mo}_2\text{C}$  exhibits metallic properties [24]. Meanwhile, the absorption curve tails up when compared to that measured on the commercial  $\text{Mo}_2\text{C}$  in the long wavelength range, which is ascribed to the existing of defects in the synthesized  $\text{Mo}_2\text{C}$  [25]. On the other hand, the absorption edges of the annealed products were significantly shifted to longer wavelengths, which suggests that the band gap opened up due to the formation of  $\text{MoO}_x$  [26]. Additionally, the Raman spectra of the products were also measured. As can be observed in Figure 2b, only weak intrinsic Raman peaks of  $\text{MoO}_x$  can be observed on the spectra collected for the materials annealed at 300 °C and 350 °C, revealing that the thermostability of  $\text{Mo}_2\text{C}$  is quite good. On the other hand, prominent Raman peaks appear on the material annealed at 400 °C. Specifically, the Raman peak which appears at 288  $\text{cm}^{-1}$  is assigned to the wagging mode of the double bond  $\text{O}=\text{Mo}=\text{O}$ , while the Raman peaks that appear at 662, 818, and 994.7  $\text{cm}^{-1}$  are assigned to the stretching mode of the triply coordinated oxygen ( $3\text{Mo}-\text{O}$ ), the doubly coordinated oxygen ( $2\text{Mo}-\text{O}$ ), and the terminal oxygen ( $\text{Mo}^{6+}-\text{O}$ ), respectively. Finally, the Raman peaks that show at 243, 286, 335, and 375  $\text{cm}^{-1}$  are indexed to the oscillation modes of ( $2\text{Mo}-\text{O}$ ), ( $\text{O}=\text{Mo}=\text{O}$ ), ( $3\text{Mo}-\text{O}$ ), and ( $\text{Mo}=\text{O}$ ), respectively [22]. The above observation demonstrates that the oxidization reaction at 400 °C is more efficient at oxidizing the  $\text{Mo}_2\text{C}$  into  $\text{MoO}_x$ . Furthermore, the SERS performance of the materials oxidized at different temperatures was investigated, and  $10^{-4}$  M R6G was used as the probe molecule. Figure 2c shows that the characteristic peaks of the R6G, from 600 to 2000  $\text{cm}^{-1}$ , could be observed on all films. In detail, the Raman peaks that appear at 608 and 772  $\text{cm}^{-1}$  are attributed to aromatic bending, and the Raman peak that is located at 1183  $\text{cm}^{-1}$  arises from aromatic C-H bending. Meanwhile, the Raman peak that shows at 1362  $\text{cm}^{-1}$  is assigned to C-C bridge stretching and, finally, the Raman peaks that appear at 1507 and 1646  $\text{cm}^{-1}$  are ascribed to aromatic C-C stretching [27]. More importantly, it also can be observed that the SERS intensities of R6G measured on the  $\text{Mo}_2\text{C}$  annealed at 300 °C and 350 °C are similar to that measured on the synthesized  $\text{Mo}_2\text{C}$ , which suggests that there is almost no change in the charge transfer capability, even when the  $\text{Mo}_2\text{C}$  has been annealed in the

air. However, it is interesting to observe that the SERS intensities of R6G measured on the  $\text{Mo}_2\text{C}$  annealed at  $400^\circ\text{C}$  are almost two times high than the intensities measured on the other two mentioned above, which reveals that the charge transfer capability of the  $\text{Mo}_2\text{C}$  annealed at  $400^\circ\text{C}$  is significantly improved.

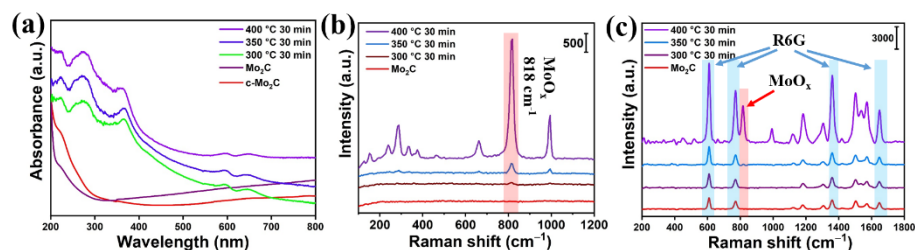


**Figure 2.** (a) The absorption curves measured on different materials that were annealed under different temperatures; (b) the corresponding Raman spectrum of the materials annealed at different temperatures; (c) the SERS spectrum of R6G measured on different materials that were annealed at different temperatures.

To further explore the effect of the annealing time on  $\text{Mo}_2\text{C}$ 's SERS performance, the synthesized  $\text{Mo}_2\text{C}$  powder was subjected to different annealing times, while the temperature was fixed at  $400^\circ\text{C}$ . As Figure 3a shows, the absorption peak blue shifts with the extension of the annealing time, which suggests that there is an increase in the amount of the  $\text{MoO}_x$  component. Meanwhile, the Raman spectra of the annealed materials and the corresponding SERS spectra of the R6G were also recorded, and these are shown in Figure 3b,c, respectively. The evolutions of the Raman peak intensities at  $818\text{ cm}^{-1}$  ( $\text{MoO}_x$ ) and  $608\text{ cm}^{-1}$  (R6G) are extracted and shown in Figure 3d. This illustrates that the characteristic Raman peaks of  $\text{MoO}_x$  gradually increase with the extension of the annealing time, which further confirms that the percentage of  $\text{MoO}_x$  increases in the products. However, the peak intensity saturates when the annealing time is  $>100$  min, indicating that the  $\text{Mo}_2\text{C}$  has been fully oxidized into  $\text{MoO}_3$ . At the same time, for the Raman peak of R6G, the Raman peak intensity gradually climbs up in the beginning, and it reaches the maximum point when the annealing time is set to 70 min. However, further increasing the annealing time degrades the material's SERS performance, and the SERS enhancement capability remains unchanged when the annealing time is  $>100$  min, which verifies that the  $\text{Mo}_2\text{C}$  is fully oxidized at that time.

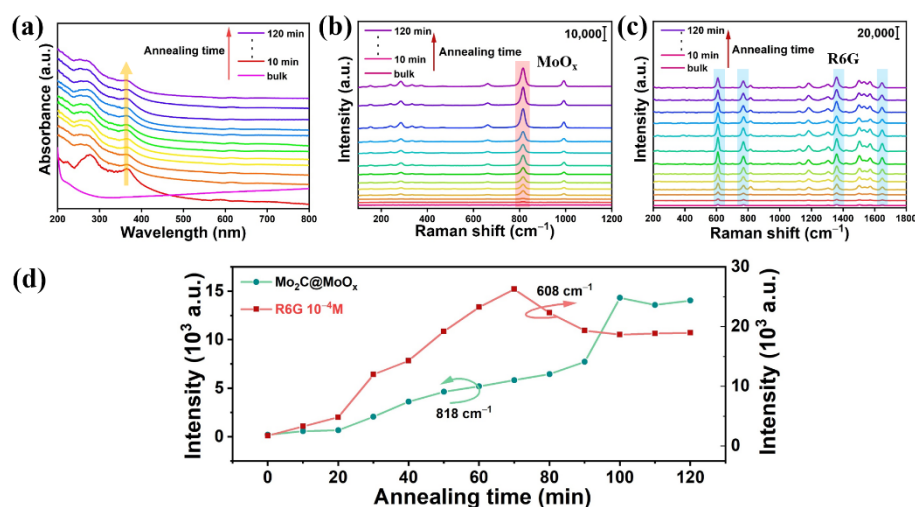


**Figure 3.** (a) The absorption curves measured; (b) the corresponding Raman spectrum; (c) the SERS spectrum of R6G measured on different samples that were annealed for different lengths of time; (d) the evolution of the Raman peak ( $818$  and  $608\text{ cm}^{-1}$ ) intensities with different annealing times.

Next, the discussion will focus on the mechanism of the SERS performance improvement observed for the  $\text{Mo}_2\text{C}$  annealed at  $400\text{ }^\circ\text{C}$  for 70 min. Firstly, SEM and TEM was used to detect the morphologies of the material. It can be seen on the SEM images in Figure 4a,b that the product still retains the irregular shapes as that of  $\text{Mo}_2\text{C}$ , but the surface becomes rough, which could be ascribed to the formation of the  $\text{MoO}_x$ . Meanwhile, the TEM image in Figure 4c,d reveals more details. It shows that the edge of the particle forms tiny antennas. In addition, the high-resolution transmission electron microscope (HRTEM) image in Figure 5d displays two lattice fringes. The first one shows d-spacing of  $2.5\text{ \AA}$ , which is consistent with the (002) plane of  $\text{Mo}_2\text{C}$ . The second one shows lattice fringes of  $1.7\text{ \AA}$ , which corresponds to the (211) plane of  $\text{MoO}_3$ . This physical evidence indicates that annealing in the air forms the  $\text{Mo}_2\text{C}@/\text{MoO}_3$  heterostructure.

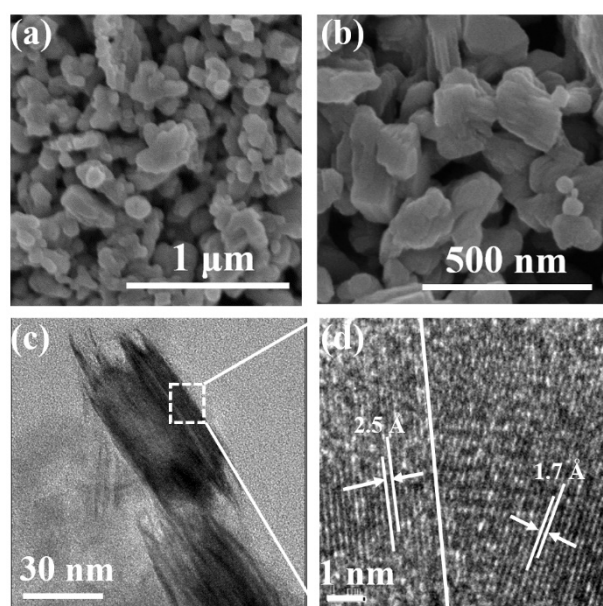


**Figure 4.** (a,b) Different magnifications of the SEM images of the  $\text{Mo}_2\text{C}$  annealed at  $400\text{ }^\circ\text{C}$  for 70 min; (c) the TEM image of the  $\text{Mo}_2\text{C}$  annealed at  $400\text{ }^\circ\text{C}$  for 70 min; (d) the corresponding high-resolution TEM image of the  $\text{Mo}_2\text{C}$  annealed at  $400\text{ }^\circ\text{C}$  for 70 min.

In addition, X-ray photoelectron spectroscopy (XPS) was used to analyze the valence states of the elements. Figure 5 shows the XPS spectra collected for the synthesized  $\text{Mo}_2\text{C}$ ,  $\text{Mo}_2\text{C}@/\text{MoO}_x$  ( $400\text{ }^\circ\text{C}$  for 70 min), and  $\text{MoO}_x$  ( $400\text{ }^\circ\text{C}$  for 100 min), respectively. Clearly, the respective peaks belonging to the Mo, O, and C atoms are observed on the element scanning spectra. Moreover, Figure 5b shows the high-resolution spectra of the Mo 3d that was measured on the synthesized  $\text{Mo}_2\text{C}$ . Three peak-shaped spectrum can be observed. Then, deconvolution analysis was performed. The two spin-orbit doublets at 227.63 and 228.33 eV can be assigned to the  $\text{Mo}^{2+}$  ion, the double peaks at 230.78 and 232.18 eV correspond to the  $\text{Mo}^{4+}$  ions, while the doublets appearing at 231.43 and 234.83 eV are indexed to the  $\text{Mo}^{5+}$  ions. Moreover, it can be attained that 42.4% of the Mo atoms are in a  $\text{Mo}^{2+}$  state, indicating that they form the  $\text{Mo}_2\text{C}$  structure. On the other hand, it also shows that the rest of the Mo ions are still in a high valence state ( $\text{Mo}^{3+}$ :28.9%,  $\text{Mo}^{4+}$ :28.7%), which reveals the possible existence of impurities (e.g.,  $\text{MoC}$ ) in the product [28]. Furthermore, the high-resolution XPS spectra of the  $\text{Mo}_2\text{C}@/\text{MoO}_x$  is shown in Figure 5d. This analysis shows that the percentage of  $\text{Mo}^{2+}$  component is reduced to 12.7% after the annealing process. Correspondingly, the percentage of Mo high valence states increases. Specifically, the percentage of  $\text{Mo}^{5+}$  ions increases to 54.0%, while  $\text{Mo}^{6+}$  ions also appear, and they make up over 33.3% of the total Mo atoms. The above change suggests that  $\text{Mo}_2\text{C}$  is partially oxidized and forms an optimal heterostructure with excellent charge transfer capabilities. The high-resolution spectra of the  $\text{MoO}_x$  are shown in Figure 5f. Clearly, a two-peak-shaped

spectrum is obtained. Through the analysis, it is found that the sample is mainly composed of  $\text{Mo}^{6+}$  ions (73.2%), while only a small percentage of the atoms are in a  $\text{Mo}^{5+}$  state (26.7%), which further confirms that the  $\text{Mo}_2\text{C}$  is completely converted to  $\text{MoO}_3$  [29]. At this time, the mechanism of the SERS enhancement observed on  $\text{Mo}_2\text{C}@MoO_x$  can be understood in Figure S2. It can be seen that the metal–semiconductor generates high levels of mixing energy in the hetero-region, the incident light produces substantial numbers of electron–hole pairs, and then the hot electrons are separated (Figure S3) and move towards the molecules because of the  $\text{MoO}_x$  energy levels, which ultimately boosts the Raman signal intensity [25,30,31].

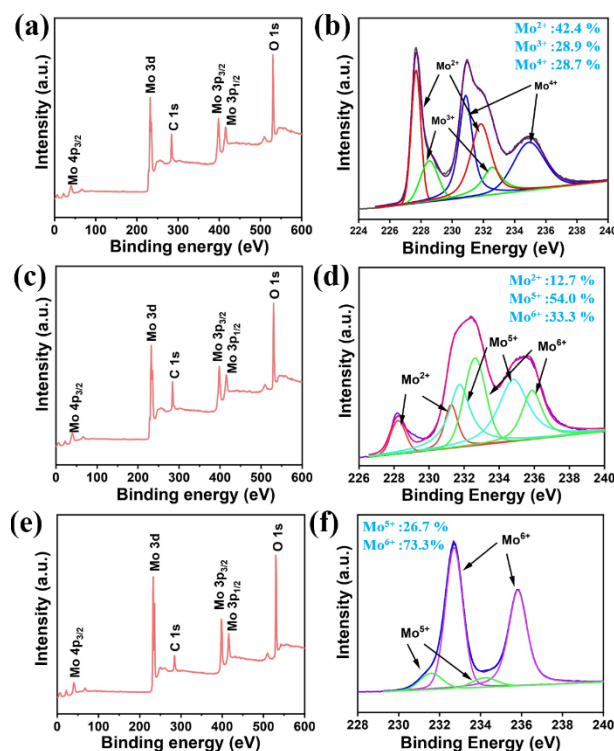


**Figure 5.** (a) The XPS element scanning spectrum measured on the synthesized  $\text{Mo}_2\text{C}$ ; (b) the high-resolution XPS scanning of the Mo 3d orbit on the synthesized  $\text{Mo}_2\text{C}$ ; (c) the XPS element scanning spectrum measured on the  $\text{Mo}_2\text{C}@MoO_x$ ; (d) the high-resolution XPS scanning of the Mo 3d orbit on the  $\text{Mo}_2\text{C}@MoO_x$ ; (e) the XPS element scanning spectrum measured on the  $\text{MoO}_3$ ; (f) the high-resolution XPS scanning of Mo 3d orbit on the  $\text{MoO}_3$ .

Finally, the sensitivity of the  $\text{Mo}_2\text{C}@MoO_x$  heterostructure was also evaluated. Figure 6a shows the collected Raman spectra when the R6G concentrations decrease from  $10^{-4}$  to  $10^{-5}$ ,  $10^{-6}$ ,  $10^{-7}$  and to  $10^{-8}$  M, respectively. Figure 6a shows that the Raman signal of the R6G is still detectable when the concentration reaches  $10^{-8}$  M, which indicates that the detection limit of the  $\text{Mo}_2\text{C}@MoO_x$  heterostructure can be as low as  $10^{-8}$  M. In addition, Figure 6b shows the logarithmic plot of the Raman peak intensity ( $608\text{ cm}^{-1}$ ) versus the R6G concentration from  $10^{-4}$  to  $10^{-8}$  M. Clearly, it can be seen that the substrate has a good linear detection capability. Other than that, the enhancement factor (EF) of the  $\text{Mo}_2\text{C}@MoO_x$  film at different R6G concentrations is also calculated by integrating the peak intensity at  $608\text{ cm}^{-1}$  (see the Supplementary Materials). It can be seen from Figure 6b that EFs of  $8.4 \times 10^5$  ( $10^{-4}$  M R6G),  $6.4 \times 10^6$  ( $10^{-5}$  M R6G),  $4.4 \times 10^7$  ( $10^{-6}$  M R6G),  $1.0 \times 10^8$  ( $10^{-7}$  M R6G), and  $1.8 \times 10^8$  ( $10^{-8}$  M R6G) can be obtained. At this moment, it is worth noting that the EF increases with the decrease in the R6G concentration, which could be ascribed to the improvement of the charge efficiency when less molecules are adsorbed on the surface. Other than that, other Raman reporters, such as methylene blue (MB), were also used. It can be seen from Figure S4 that the substrate shows excellent Raman enhancement capabilities.

Moreover, the LoD can reach  $10^{-8}$  M, as well. Furthermore, the uniformity of the Raman signal intensity on the  $\text{Mo}_2\text{C}@\text{MoO}_x$  heterostructure was evaluated. To achieve this, the Raman signal intensity map was recorded for the  $\text{Mo}_2\text{C}@\text{MoO}_x$  substrate. Specifically, a randomly selected square of  $80 \times 80 \mu\text{m}^2$  was used for the mapping measurement. In the measurement,  $10^{-4}$  M R6G was used as the reporter and a total of 1600 points were collected. Figure 6c shows the intensity mapping of the Raman peak at  $608 \text{ cm}^{-1}$ . The figure shows good Raman signal intensity for a large-scale area. In addition, the statistical data in Figure 6d show that the average mapping intensity is 7004.5 cps, while the relative standard derivative (RSD) is calculated to be 13.02%. The above data indicate that the prepared  $\text{Mo}_2\text{C}@\text{MoO}_x$  substrate has excellent uniformity. Finally, as the literature reported that both  $\text{Mo}_2\text{C}$  and  $\text{MoO}_x$  have relatively good resistance to high temperatures and acidic/alkaline environments, it is expected that the  $\text{Mo}_2\text{C}@\text{MoO}_x$  heterostructure-based SERS substrate can expand the potential application fields for multipurpose detection [21,25].

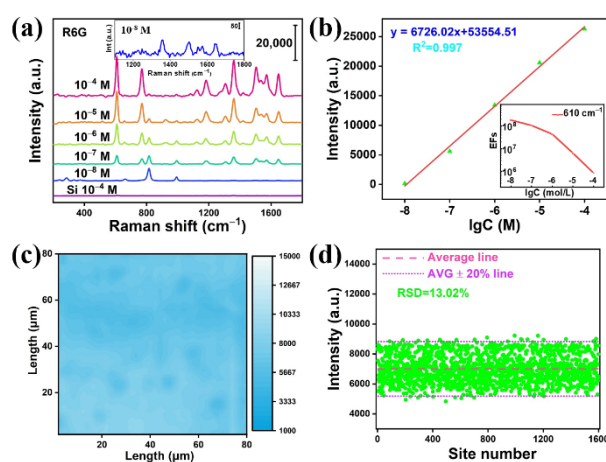


**Figure 6.** (a) The SERS spectrum of the R6G measured with different concentrations; (b) the logarithmic plot of the Raman peak ( $608 \text{ cm}^{-1}$ ) intensity versus different R6G concentrations; (c) the Raman peak ( $608 \text{ cm}^{-1}$ ) intensity mapping; (d) the statistical data of the mapped data points.

#### 4. Conclusions

To summarize, a type of  $\text{Mo}_2\text{C}@\text{MoO}_x$  heterostructure has been finely prepared, and improved SERS performance has been achieved through the heterostructure-induced charge transfer. Specifically, attractive SERS performance with a Raman enhancement factor (EF) of  $1.445 \times 10^8$  ( $\text{R6G}@10^{-8}$  M) and a limit of detection of  $10^{-8}$  M has been achieved. Furthermore, the mechanism of the SERS performance improvement was also investigated. HRTEM detection and XPS spectra revealed that part of the  $\text{Mo}_2\text{C}$  is partially oxidized into  $\text{MoO}_x$ , and generates metal–semiconductor mixing energy bands in the heterojunction. Under Raman laser irradiation, a considerable number of hole–electron pairs are generated in the heterojunction, and then the hot electrons move towards  $\text{MoO}_x$  and subsequently transfer to the molecules, which ultimately boosts the Raman signal intensity.

**Supplementary Materials:** The following supporting information can be downloaded at: <https://www.mdpi.com/article/10.3390/bios12020050/s1>, Figure S1: The optical and cross-section SEM image of the deposited  $\text{Mo}_2\text{C}$  film; Figure S2: The charge transfer path; Figure S3: PL spectra measured on  $\text{Mo}_2\text{C}$  and  $\text{Mo}_2\text{C}@\text{MoO}_x$ ; Figure S4: SERS spectra of MB; Note 1: calculation of the enhancement factor.

**Author Contributions:** A.C. and C.G. designed the experiment; K.L., K.Y. and Q.Y. prepared the samples and performed the characterizations. K.L. and D.C. (Dong Chen) drafted the manuscript; A.C. and D.C. (Da Chen) reviewed and finalized the manuscript. All authors have read and agreed to the published version of the manuscript.



**Funding:** This research was supported by the Key Research and Development Program of Zhejiang Province (Grant No: 2020C03026), the Fundamental Research Funds for the Provincial Universities of Zhejiang, and the K.C. Wong Magna Fund in Ningbo University.

**Data Availability Statement:** The data presented in this study are available in article or supplementary material.

**Acknowledgments:** The author would acknowledge the facilitating support from Ningbo University.

**Conflicts of Interest:** The authors declare no conflict of interest.

## References

1. Langer, J.; Jimenez de Aberasturi, D.; Aizpurua, J.; Alvarez-Puebla, R.A.; Auguie, B.; Baumberg, J.J.; Bazan, G.C.; Bell, S.E.J.; Boisen, A.; Brolo, A.G.; et al. Present and future of surface-enhanced Raman scattering. *ACS Nano* **2020**, *14*, 28–117. [[CrossRef](#)]
2. Tian, Y.; Liu, H.; Chen, Y.; Gu, C.; Wei, G.; Jiang, T. Quantitative SERS-based detection and elimination of mixed hazardous additives in food mediated by the intrinsic Raman signal of TiO<sub>2</sub> and magnetic enrichment. *ACS Sustain. Chem. Eng.* **2020**, *8*, 16990–16999. [[CrossRef](#)]
3. Liu, C.; Yang, M.; Yu, J.; Lei, F.; Wei, Y.; Peng, Q.; Li, C.; Li, Z.; Zhang, C.; Man, B. Fast multiphase analysis: Self-separation of mixed solution by a wettability-controlled CuO@Ag SERS substrate and its applications in pollutant detection. *Sens. Actuators B Chem.* **2020**, *307*, 127663. [[CrossRef](#)]
4. Ben-Jaber, S.; Peveler, W.J.; Quesada-Cabrera, R.; Cortés, E.; Sotelo-Vazquez, C.; Abdul-Karim, N.; Maier, S.A.; Parkin, I.P. Photo-induced enhanced Raman spectroscopy for universal ultra-trace detection of explosives, pollutants and biomolecules. *Nat. Comm.* **2016**, *7*, 12189. [[CrossRef](#)] [[PubMed](#)]
5. Xu, K.; Zhou, R.; Takei, K.; Hong, M. Toward flexible surface-enhanced Raman scattering (SERS) sensors for point-of-care diagnostics. *Adv. Sci.* **2019**, *6*, 1900925. [[CrossRef](#)]
6. Ning, C.-F.; Wang, L.; Tian, Y.-F.; Yin, B.-C.; Ye, B.-C. Multiple and sensitive SERS detection of cancer-related exosomes based on gold–silver bimetallic nanotrepangs. *Analyst* **2020**, *145*, 2795–2804. [[CrossRef](#)] [[PubMed](#)]
7. Mosier-Boss, P.A. Review of SERS substrates for chemical sensing. *Nanomaterials* **2017**, *7*, 142. [[CrossRef](#)] [[PubMed](#)]
8. Pérez-Jiménez, A.I.; Lyu, D.; Lu, Z.; Liu, G.; Ren, B. Surface-enhanced Raman spectroscopy: Benefits, trade-offs and future developments. *Chem. Sci.* **2020**, *11*, 4563–4577. [[CrossRef](#)] [[PubMed](#)]
9. Lee, H.K.; Lee, Y.H.; Koh, C.S.L.; Phan-Quang, G.C.; Han, X.; Lay, C.L.; Sim, H.Y.F.; Kao, Y.-C.; An, Q.; Ling, X.Y. Designing surface-enhanced Raman scattering (SERS) platforms beyond hotspot engineering: Emerging opportunities in analyte manipulations and hybrid materials. *Chem. Rev.* **2019**, *48*, 731–756. [[CrossRef](#)] [[PubMed](#)]
10. Ma, Y.; Du, Y.; Chen, Y.; Gu, C.; Jiang, T.; Wei, G.; Zhou, J. Intrinsic Raman signal of polymer matrix induced quantitative multiphase SERS analysis based on stretched PDMS film with anchored Ag nanoparticles/Au nanowires. *Chem. Eng. J.* **2020**, *381*, 122710. [[CrossRef](#)]
11. Tan, L.-L.; Wei, M.; Shang, L.; Yang, Y.-W. Cucurbiturils-mediated noble metal nanoparticles for applications in sensing, SERS, theranostics, and catalysis. *Adv. Funct. Mater.* **2021**, *31*, 2007277. [[CrossRef](#)]
12. Wei, W.; Du, Y.; Zhang, L.; Yang, Y.; Gao, Y. Improving SERS hot spots for on-site pesticide detection by combining silver nanoparticles with nanowires. *J. Mater. Chem. C* **2018**, *6*, 8793–8803. [[CrossRef](#)]
13. Li, M.; Fan, X.; Gao, Y.; Qiu, T. W<sub>18</sub>O<sub>49</sub>/monolayer MoS<sub>2</sub> heterojunction-enhanced Raman scattering. *J. Phys. Chem. Lett.* **2019**, *10*, 4038–4044. [[CrossRef](#)]
14. Zhou, C.; Sun, L.; Zhang, F.; Gu, C.; Zeng, S.; Jiang, T.; Shen, X.; Ang, D.S.; Zhou, J. Electrical tuning of the SERS enhancement by precise defect density control. *ACS Appl. Mater. Interfaces* **2019**, *11*, 34091–34099. [[CrossRef](#)] [[PubMed](#)]
15. Cheng, R.; Hu, T.; Hu, M.; Li, C.; Liang, Y.; Wang, Z.; Zhang, H.; Li, M.; Wang, H.; Lu, H.; et al. MXenes induce epitaxial growth of size-controlled noble nanometals: A case study for surface enhanced Raman scattering (SERS). *J. Mater. Res. Technol.* **2020**, *40*, 119–127. [[CrossRef](#)]
16. Yang, L.; Gong, M.; Jiang, X.; Yin, D.; Qin, X.; Zhao, B.; Ruan, W. Investigation on SERS of different phase structure TiO<sub>2</sub> nanoparticles. *J. Raman Spectrosc.* **2015**, *46*, 287–292. [[CrossRef](#)]
17. Zhou, X.; Wu, D.; Jin, Z.; Song, X.; Wang, X.; Suib, S.L. Significantly increased Raman enhancement on defect-rich O-incorporated 1T-MoS<sub>2</sub> nanosheets. *J. Mater. Sci.* **2020**, *55*, 16374–16384. [[CrossRef](#)]
18. He, R.; Lai, H.; Wang, S.; Chen, T.; Xie, F.; Chen, Q.; Liu, P.; Chen, J.; Xie, W. Few-layered vdW MoO<sub>3</sub> for sensitive, uniform and stable SERS applications. *Appl. Surf. Sci.* **2020**, *507*, 145116. [[CrossRef](#)]
19. Jing, X.-X.; Li, D.-Q.; Zhang, Y.; Hou, X.-Y.; Jiang, J.; Fan, X.-C.; Wang, M.-C.; Feng, S.-P.; Yu, Y.-f.; Lu, J.-P.; et al. Surface-enhanced Raman scattering of hydrogen plasma-treated few-layer MoTe<sub>2</sub>. *Chin. Phys. Lett.* **2021**, *38*, 074203. [[CrossRef](#)]
20. Jiang, J.; Liu, H.; Li, X.; Chen, Y.; Gu, C.; Wei, G.; Zhou, J.; Jiang, T. Nonmetallic SERS-based immunosensor by integrating MoS<sub>2</sub> nanoflower and nanosheet towards the direct serum detection of carbohydrate antigen 19-9. *Biosens. Bioelectron.* **2021**, *193*, 113481. [[CrossRef](#)] [[PubMed](#)]
21. Zhang, Q.; Li, X.; Ma, Q.; Zhang, Q.; Bai, H.; Yi, W.; Liu, J.; Han, J.; Xi, G. A metallic molybdenum dioxide with high stability for surface enhanced Raman spectroscopy. *Nat. Comm.* **2017**, *8*, 14903. [[CrossRef](#)] [[PubMed](#)]

22. Xie, S.; Chen, D.; Gu, C.; Jiang, T.; Zeng, S.; Wang, Y.Y.; Ni, Z.; Shen, X.; Zhou, J. Molybdenum oxide/tungsten oxide nano-heterojunction with improved surface-enhanced Raman scattering performance. *ACS Appl. Mater. Interfaces* **2021**, *13*, 33345–33353. [[CrossRef](#)]
23. Wu, C.M.; Naseem, S.; Chou, M.-H.; Wang, J.; Jian, Y. Recent Advances in Tungsten-Oxide-Based Materials and Their Applications. *Front. Mater. Sci.* **2019**, *6*, 49. [[CrossRef](#)]
24. Kang, Z.; Cheng, Y.; Zheng, Z.; Cheng, F.; Chen, Z.; Li, L.; Tan, X.; Xiong, L.; Zhai, T.; Gao, Y. MoS<sub>2</sub>-based photodetectors powered by asymmetric contact structure with large work function difference. *Nanomicro Lett.* **2019**, *11*, 34. [[CrossRef](#)] [[PubMed](#)]
25. Yang, L.; Chen, W.; Yang, R.; Chen, A.; Zhang, H.; Sun, Y.; Jia, Y.; Li, X.; Tang, Z.; Gui, X. Fabrication of MoO<sub>x</sub>/Mo<sub>2</sub>C-layered hybrid structures by direct thermal oxidation of Mo<sub>2</sub>C. *ACS Appl. Mater. Interfaces* **2020**, *12*, 10755–10762. [[CrossRef](#)] [[PubMed](#)]
26. Wu, H.; Wang, H.; Li, G. Metal oxide semiconductor SERS-active substrates by defect engineering. *Analyst* **2017**, *142*, 326–335. [[CrossRef](#)]
27. Zhang, C.; Jiang, S.Z.; Huo, Y.Y.; Liu, A.H.; Xu, S.C.; Liu, X.Y.; Sun, Z.C.; Xu, Y.Y.; Li, Z.; Man, B.Y. SERS detection of R6G based on a novel graphene oxide/silver nanoparticles/silicon pyramid arrays structure. *Opt. Express* **2015**, *23*, 24811–24821. [[CrossRef](#)]
28. Cui, W.; Cheng, N.; Liu, Q.; Ge, C.; Asiri, A.M.; Sun, X. Mo<sub>2</sub>C nanoparticles decorated graphitic carbon sheets: Biopolymer-derived solid-state synthesis and application as an efficient electrocatalyst for hydrogen generation. *ACS Catal.* **2014**, *4*, 2658–2661. [[CrossRef](#)]
29. Gu, C.; Li, D.; Zeng, S.; Jiang, T.; Shen, X.; Zhang, H. Synthesis and defect engineering of molybdenum oxides and their SERS applications. *Nanoscale* **2021**, *13*, 5620–5651. [[CrossRef](#)] [[PubMed](#)]
30. Wu, K.; Chen, J.; McBride, J.R.; Lian, T. Efficient hot-electron transfer by a plasmon-induced interfacial charge-transfer transition. *Science* **2015**, *349*, 632–635. [[CrossRef](#)]
31. Jing, X.; Peng, X.; Sun, X.; Zhou, W.; Wang, W.; Wang, S. Design and synthesis of Mo<sub>2</sub>C/MoO<sub>3</sub> with enhanced visible-light photocatalytic performance for reduction of Cr (VI) and degradation of organic pollutants. *Mater. Sci. Semicond. Process.* **2019**, *100*, 262–269. [[CrossRef](#)]